journal of the mechanical behavior of biomedical materials 136 (2022) 105529

Contents lists available at ScienceDirect

Journal of the Mechanical Behavior of Biomedical Materials

journal homepage: www.elsevier.com/locate/jmbbm

Hierarchical modeling of elastic moduli of equine hoof wall

Cheng-Shen (Andrew) Shiang [a,1], Christian Bonney [a,1], Benjamin Lazarus [b], Marc Meyers [b,c,d], Iwona Jasiuk [a,*]

[a] Dept. of Mechanical Science and Engineering, University of Illinois, Urbana-Champaign, USA
[b] Materials Science and Engineering Program, University of California, San Diego, USA
[c] Dept. of Mechanical and Aerospace Engineering, University of California, San Diego, USA
[d] Dept. of Nanoengineering, University of California, San Diego, USA

ARTICLE INFO

Keywords:
Equine hoof wall
Keratin
Elastic moduli
Modeling
Structural hierarchy

ABSTRACT

This study predicts analytically effective elastic moduli of substructures within an equine hoof wall. The hoof wall is represented as a composite material with a hierarchical structure comprised of a sequence of length scales. A bottom-up approach is employed. Thus, the outputs from a lower spatial scale serve as the inputs for the following scale. The models include the Halpin-Tsai model, composite cylinders model, a sutured interface model, and classical laminate theory. The length scales span macroscale, mesoscale, sub-mesoscale, microscale, sub-microscale, and nanoscale. The macroscale represents the hoof wall, consisting of tubules within a matrix at the mesoscale. At the sub-mesoscale, a single hollow tubule is reinforced by a tubule wall made of lamellae; the surrounding intertubular material also has a lamellar structure. The lamellae contain sutured and layered cells at the microscale. A single cell is made of crystalline macrofibrils arranged in an amorphous matrix at the sub-microscale. A macrofibril contains aligned crystalline rod-like intermediate filaments at the nanoscale. Experimentally obtained parameters are used in the modeling as inputs for geometry and nanoscale properties. The predicted properties of the hoof wall material agree with experimental measurements at the mesoscale and macroscale. We observe that the hierarchical structure of the hoof wall leads to a decrease in the elastic modulus with increasing scale, from the nanoscale to the macroscale. Such behavior is an intrinsic characteristic of hierarchical biological materials. This study can serve as a framework for designing impact-resistant hoof-inspired materials and structures.

1. Introduction

Engineers aim to design new structural materials with superior performance, such as high specific stiffness, strength, fracture toughness, and energy absorption. These technological advancements are achieved by synthesizing new materials or creating new architectures and composites using existing materials. Biological materials are a rich source of inspiration for new structural designs. Strategies found in nature have already been implemented with great success. Examples include bullet trains in Japan taking inspiration from swallows, the Taipei 101 skyscraper taking inspiration from bamboo, and the Beijing National Stadium taking inspiration from bird nests. Another natural structure that is worth studying and taking inspiration from is the equine hoof, which consists of a load-bearing shell (the hoof wall) encircling much softer tissue.

The equine hoof wall experiences massive dynamic loads under the horse's weight in full gallop. The hoof wall is only about 10–15 mm thick, yet horses can reach weights of 900 kg generating large stresses in the hoof capsule. Depending on the impact surface, horse hooves can experience between 27 g and 84 g of acceleration (Lanovaz et al., 1998; Setterbo et al., 2009). Interestingly, equine hooves have no mineralized constituents but can handle these high repeated impacts.

The hoof wall is made of a biopolymer called keratin. Keratin is also present in natural systems such as skins, horns, hair, claws, and scales (McKittrick et al., 2012; Meyers et al., 2008; Wang et al., 2016a). Keratin is classified into two types, α- and β-keratin. Typically, α-keratin is found in mammals, while β-keratin is found in avians and reptiles (Toni et al., 2007). At the atomic level, keratin is made of amino acid chains, in

---

[*] Corresponding author. Department of Mechanical Science and Engineering University of Illinois Urbana-Champaign, 1206 West Green Street Urbana, IL, 61801, USA.

E-mail address: ijasiuk@illinois.edu (I. Jasiuk).

[1] The authors contributed equally to this paper.

https://doi.org/10.1016/j.jmbbm.2022.105529
Received 15 August 2022; Received in revised form 9 October 2022; Accepted 14 October 2022
Available online 23 October 2022

which the α-keratin forms a right-handed α-helix, while the β-keratin protein structure has a β-pleated sheet form (Fraser and MacRae, 1983). Keratin's mechanical properties depend not only on its molecular structure but also on the amino acid composition and hydration level.

The equine hoof wall is made of α-keratin and is most similar in nanostructure and composition to the keratin found in hair, nails, and horns (Marshall et al., 1991). The fundamental structure of these materials is a crystalline fiber called an intermediate filament (IF), which is embedded in an amorphous sulfur-based protein matrix (McKittrick et al., 2012). Despite a similar nanostructure, keratins can differ widely in their overall architectures and mechanical behavior. For example, human hair ($E_{50\%\ \text{relative humidity}} = 4.2$ GPa) is characterized by an outside cuticle structure with a cortex composed of long keratinocyte cells surrounding aligned fibers that maximize tensile strength (Yu et al., 2017) and insulation (Cui et al., 2018) while pangolin scales ($E_{50\%\ \text{relative humidity}} = 0.963$ GPa) contain a cross-lamellar structure that redirects cracks away from the scale's interior (Wang et al., 2016b). Likewise, the hoof wall has a hierarchical structure that enhances its functionality with distinct features at each scale. Within their hierarchical structure, equine hooves contain features commonly identified in other impact-resistant biological systems, including tubules, layers, and sutured interfaces (Kasapi and Gosline, 1997, 1999; Lazarus et al., 2021).

Tubules are long hollow channels that are characteristic of several biological materials. In the hoof wall, the tubules are separated by a softer intertubular matrix and have stiff outer walls that act as reinforcement. Tubules are also found in teeth, whale baleen, alligator gar scales, horn, insect forewings, and plant-based systems like wood. Other natural materials such as bone and elk antlers have tubular structures called osteons. Tests on these natural systems show that tubules can toughen a material by deflecting cracks at interfaces, confining cracks, or absorbing strain energy (Huang, 2018; Launey et al., 2010; Matsushita et al., 2020; Wang et al., 2019). Studies have confirmed the beneficial attributes of tubules, particularly for impact resistance, via 3D printing (Chen et al., 2018; Wang et al., 2021) and parametric numerical analyses (Hao and Du, 2018; Ma et al., 2021; Tsang and Raza, 2018; Zhang et al., 2018).

Lamellar structures are also common in natural materials including bone, conch shells, woodpecker skulls, mantis shrimp dactyl clubs, pangolin scales, and nacre (Lazarus et al., 2020; Lin and Meyers, 2005). Like tubules, lamellae deflect cracks and absorb energy when they delaminate (Lee et al., 2011). Thus, researchers have studied these structures through bioinspired designs (Grunenfelder et al., 2014; Gu et al., 2017; Islam et al., 2022; Jia et al., 2019; Rice and Tan, 2019) and numerical modeling (Ghazlan et al., 2016; Miranda et al., 2019).

Sutures also occur frequently within biological materials to join neighboring components. Sutures are composite regions characterized by stiff interdigitating serrations separated by a softer interface material. They are seen between bony plates of the human skull (Brown et al., 2020), boxfish scutes (Yang et al., 2015), turtle carapace (Achrai and Wagner, 2013; Chen et al., 2015), and at cellular interfaces of pangolin scales (Wang et al., 2016b) and equine hooves (Kasapi and Gosline, 1999). The Ortiz group studied sutures with regular waveforms by exploring parameters such as shape, degree of interdigitation, material properties, interface bonding, and suture hierarchies (Li et al., 2011, 2012). They tested 3D printed sutured composites and obtained in-plane stiffness, strength, fracture toughness, and failure mechanisms (Lin et al., 2014a, 2014b). Others studied suture interfaces in nature (Chen et al., 2015; Ampaw et al., 2019; Dunlop et al., 2011; Jiang et al., 2020; Rivera et al., 2020) and developed models (Cordisco et al., 2012, 2014; Liu et al., 2017, 2020). Still, few studies looked at sutured interfaces at the cellular level or as a single component of a hierarchical structure.

Orientations in various locations in the hoof wall are described by longitudinal, radial, and circumferential directions. As seen in Fig. 1, the longitudinal direction describes the distal-proximal direction parallel with the outer wall, which is at a 40–50-degree angle with the hoof's sole. The circumferential direction denotes the direction along the hoof wall's circumference and is stratified into three sections: medial, toe, and lateral. Finally, the radial direction specifies the region through the thickness of the hoof varying from the stratum internum to the stratum externum (Kasapi and Gosline, 1997; Huang et al., 2019).

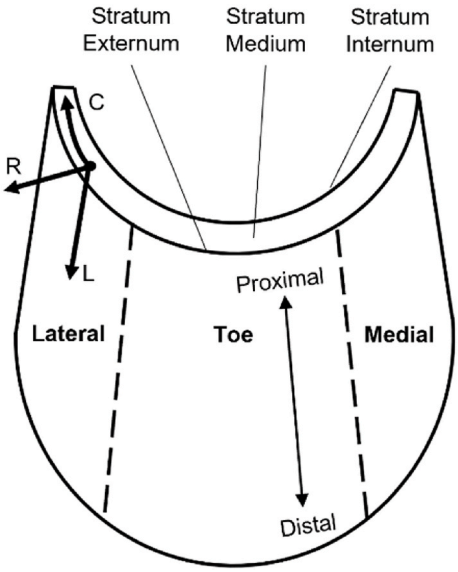

Fig. 1. Coordinate directions and locations for a right equine hoof wall. L, R, and C stand for the longitudinal, radial, and circumferential directions.

This study utilizes inputs from existing experimental data to predict the effective elastic moduli of an equine hoof wall at distinct structural levels. Each level is modeled as a two-phase composite. The effective elastic properties of the homogenized composite serve as the inputs for the following level. Similar studies of multileveled hierarchical structures used asymptotic homogenization (Dimitrienko et al., 2015; Ramírez-Torres et al., 2018, 2019) and average field techniques (Kwon and Clumpner, 2018; Piat and Schnack, 2003; Hamed et al., 2010) to compute the effective elastic constants for each scale. Our approach is similar to the average field techniques used by Hamed et al. (2010), who modeled each successive scale of bone with linear elastic micromechanical models. Each structural level of the hoof wall is represented by a micromechanical composite material model specific to the relevant geometry of the microstructure at that length scale.

The predicted elastic moduli of the hoof wall at the macroscale and mesoscale are compared with experimental data. Linear elastic models describe each hierarchical level so they can later be generalized to models accounting for hyperelastic or viscoelastic constitutive responses that are more representative of the hoof wall's behavior (Shahkhosravi et al., 2021). Hierarchical modeling also provides insights into the mechanical behavior of structures in the hoof wall at lower scales that are challenging to test experimentally.

In Section 2, the hoof wall structure is stratified into hierarchical levels and each level is described. Section 3 presents the analytical models chosen for each length scale, while Section 4 describes the models' experimental inputs and assumptions. The subsequent sections present the predictions, discuss the model outputs, and compare them to experimental results.

2. Structure of the hoof wall

Biological materials are constructed by a self-assembly process that begins at atomic to molecular levels. Natural materials have complex features which transition continuously across many length scales. One of the main challenges of hierarchically modeling biological materials is deciding how to discretize sub-structures such that the models are sufficiently representative. For this analysis, the hoof wall has been divided into six structural scales (nanoscale, sub-microscale, microscale, sub-mesoscale, mesoscale, and macroscale), representing distinct features as shown in Fig. 2. The seventh length scale is the system level, the hoof. We model an equine hoof wall from the nanoscale to macroscale levels (see Fig. 2).

The nanoscale represents an intermediate filament, IF, embedded in an amorphous matrix. The IFs consist of polypeptide chains that are formed by the α-keratin amino acids (Lazarus et al., 2021; Crick, 1952). One can construct a hierarchical model for α-keratin that begins on the molecular level. However, using a bottom-up approach, the mechanical behavior of the smallest scale must be known. The nanoscale is a convenient starting point due to the availability of experimental tension data for isolated IFs. The IFs assemble into larger diameter fibers, known as macrofibrils (Fraser and MacRae, 1983), at the sub-microscale.

At the microscale, keratinocyte cells contain many aligned macrofibrils (Huang et al., 2019). These cells join via sutured interfaces (Wang et al., 2016b; Kasapi and Gosline, 1999). In the hoof wall, there are two distinct keratinocyte shapes. They resemble flat, irregular polygons with one dimension much smaller than the others in the tubular walls. However, in the intertubular region of the hoof wall, the cells have roughly equal dimensions in all directions, making them appear globular rather than flat (Huang et al., 2019).

The sub-mesoscale is defined by lamellae, consisting of many sutured cells, that stack to form a layered structure (Kasapi and Gosline, 1999; Lazarus et al., 2020). In the tubule walls, lamellae concentrically surround the medullary cavities of the tubules creating a cortical or tubular region (Leach, 1980). In this zone, aligned fibers in the cells helically wind around the tubules. In contrast, lamellae in the intertubular region are straight, and their orientation changes through the thickness of the hoof wall. At the innermost section of the hoof wall, the intertubular layers are almost perpendicular to the tubules, while the layers close to the hoof's exterior are approximately parallel to the tubules. This change in the layer orientation is believed to divert cracks from propagating towards the soft tissue of the hoof and enhance fracture toughness by directing cracks along lamellar interfaces (Kasapi and Gosline, 1997; Bertram and Gosline, 1986; Wang et al., 2020a, 2020b).

The mesoscale is dominated by the elliptical tubular structures of the hoof. Unlike tubules found in other keratins, such as the horns of bighorn sheep, the hoof's tubules have a reinforced tubule wall surrounding the medullary cavity (Huang et al., 2019; Johnson et al., 2017). It has been suggested that this region is stiffer due to fiber alignment, higher IF density, higher crystallinity, or a combination of all three. These structures support the hoof in the longitudinal direction and absorb energy through buckling.

3. Modeling

The analytical models for each length scale are composite material models that take the properties of the constituent materials as inputs and give the homogenized properties of the composite as the outputs. Five levels of modeling were employed to describe the relationship between the effective elastic properties of the six structural scales from the nanoscale to macroscale. In this section, the models chosen for each scale are discussed.

3.1. Nanoscale and sub-microscale

The first two scales can be modeled as fibers embedded in a matrix. The nanoscale model gives the effective properties of a macrofibril and the sub-microscale model gives the effective properties of a keratin cell, as shown in Fig. 3. The semi-empirical Halpin-Tsai model, based on the self-consistent method, was applied to both scales using the following equations (Halpin, 1969; Halpin and Kardos, 1976; Osoka and Onukwuli, 2018):

$$P_c = P_0\left(\frac{1+\zeta\eta f_1}{1-\eta f_1}\right) \tag{1}$$

$$\eta = \frac{\frac{P_1}{P_0}-1}{\frac{P_1}{P_0}+\zeta} \tag{2}$$

where P represents a given elastic constant, f is the volume fraction, and the subscripts 1, 0, and c denote the fiber, matrix, and composite. The value of ζ depends on the elastic property in question, as shown in Table 1, where l and D_f are the length and diameter of the fibers. The subscripts L and T denote the longitudinal and transverse properties of the material.

3.2. Microscale

The microscale suture interface model computes the properties of a

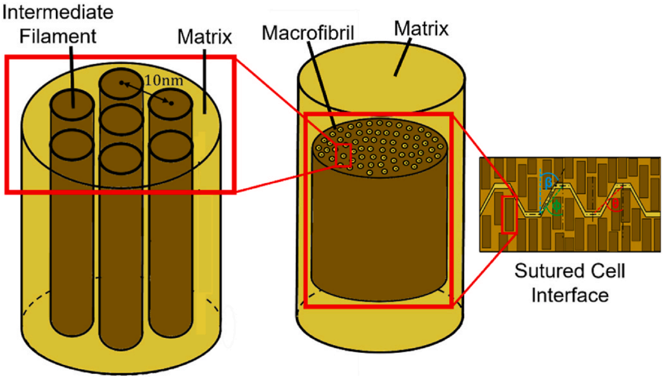

Fig. 3. Hierarchical arrangement of keratin fibers.

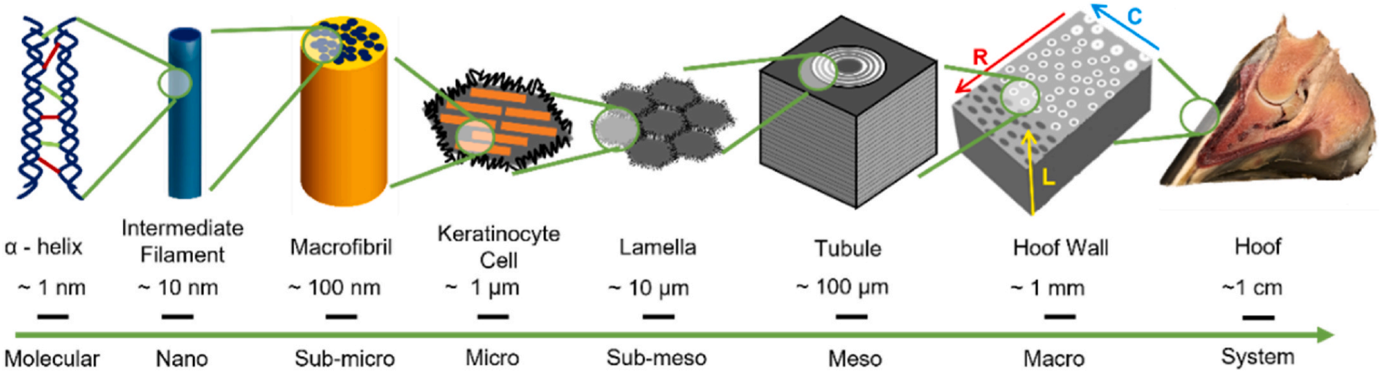

Fig. 2. Hierarchical structure of the hoof wall.

Table 1
The Halpin-Tsai model parameters.

P	ζ
Longitudinal Elastic Modulus (E_L)	$\frac{2l}{D_f}$
Transverse Elastic Modulus (E_T)	0.5
Longitudinal Shear Modulus (G_L)	1
Longitudinal Poisson's Ratio (ν_L)	∞

lamella, from the properties and geometry of the cells and interface material. A model for the elastic behavior of sutures developed by Li et al. (2013) was used in this analysis. The important geometric parameters for this model are illustrated in Fig. 4. The volume fraction of the serrations (f_1), serration angle (θ), and shape factor (β) are the independent geometric parameters. The remaining terms are derived from those three parameters. The model accounts for trapezoidal or triangular interfaces since the waveform is triangular when β = θ.

The equations for calculating the effective elastic moduli of the interfaces in tension are shown below; Eqns. (3)–(5). The subscripts 0, 1, and C denote the interface, cells, and homogenized composite. E_0^{PS} represents the plane strain elastic modulus of the interface material.

$$E_c = f_1\left[\left(\frac{1}{f_1}-1\right)tan^2\,\theta\left(\frac{cos^2\,\beta\,sin^2\,\beta}{E_0^{PS}}+\frac{cos^4\,\beta}{G_0}\right)+\frac{\zeta(\beta,\theta)}{E_1}\right] \tag{3}$$

$$\zeta(\beta,\theta)=\begin{cases} 1 \quad if\ \beta=\theta \\ \dfrac{2\ tan\ \theta}{3\ tan\ \varphi} \quad if\ \beta=0 \\ 2\dfrac{tan\ \theta}{tan\ \varphi}\left[0.5a-a+a^2\ln\left(1+\dfrac{1}{a}\right)\right] \quad if\ \beta\in(-\theta,0)\cup(0,\theta) \end{cases} \tag{4}$$

$$a=\frac{tan\ \varphi}{tan\ \beta}-1 \tag{5}$$

These equations are used to calculate both the longitudinal and transverse elastic moduli of the lamellae. In the first case, the elastic modulus of the serrations (E_1) is equal to the cells' longitudinal modulus, and in the second case, the transverse modulus of the cells is used instead, both of which are the outputs of the sub-microscale Halpin-Tsai model.

The shear modulus of the lamella is calculated using Eqns. (6)–(9). G_s is the average shear modulus of the two phases.

$$G_L=\frac{f_1^2E_0E_1C'}{f_1E_0C'C^b+E_1(1-f_1)tan^2\,\theta+E_1tan\theta\ tan\ \beta\ C^r} \tag{6}$$

$$C^b=\frac{3E_1}{4G_s}+\frac{5}{16}(\tan\theta)^{-2} \tag{7}$$

$$C^r=\frac{3G_0}{2G_s}+\frac{9G_0}{8E_1}(\tan\theta)^{-2} \tag{8}$$

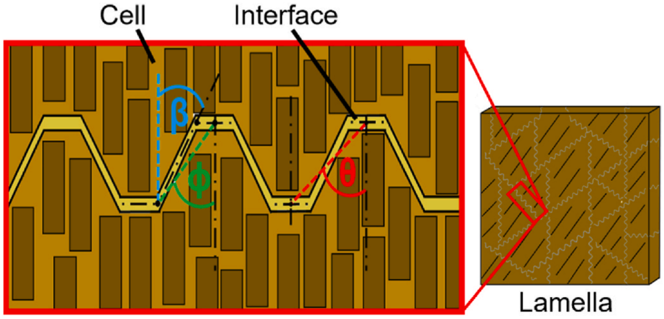

Fig. 4. Sutured cell interface within lamella.

$$C'=\frac{G_0}{E_0}tan^2\,\beta+\frac{E_0^{PS}}{E_0} \tag{9}$$

3.3. Sub-mesoscale

The lamellae form a concentric multi-layered structure around the tubules at the sub-mesoscale, as shown in Fig. 5. In this structure, the fibers are helically arranged around the tubule. The angle between the tubule's axis and the fiber direction of a lamella is called the winding angle (α). The winding directions of some lamellae are clockwise while others wind counterclockwise. The tubule walls in the middle of the hoof have about eight layers. The layers closest to the medullary cavity and the outer layers have the highest winding angles while those in-between have lower angles (Kasapi and Gosline, 1997). In this way, the tubule walls resemble a symmetric, balanced laminate which can be modeled using a classical laminate theory (CLT) (Azzi and Tsai, 1965; Christensen, 2012; Hyer and White, 2009). The reduced stiffness matrix of a single lamella is calculated from the elastic constants produced by the suture interface model. By considering the most extreme winding angles present in the hoof wall, CLT can provide upper and lower bound estimates for the longitudinal tensile modulus of the tubule wall.

The general form of CLT is given in Eqn. (10), following the notation in (Hyer and White, 2009), where [A] stands for laminate extensional stiffness, [B] is laminate coupling stiffness, and [D] is laminate bending stiffness. These matrices relate the force and moment resultants, N and M, to the extensional strain, $\boldsymbol{\varepsilon}$, and curvature, $\boldsymbol{\kappa}$, of the laminate.

$$\begin{matrix} N_x \\ N_y \\ N_{xy} \\ M_x \\ M_y \\ M_{xy} \end{matrix} = \begin{bmatrix} A_{11} & A_{12} & A_{16} & B_{11} & B_{12} & B_{16} \\ A_{12} & A_{22} & A_{26} & B_{12} & B_{22} & B_{26} \\ A_{16} & A_{26} & A_{66} & B_{16} & B_{26} & B_{66} \\ B_{11} & B_{12} & B_{16} & D_{11} & D_{12} & D_{16} \\ B_{12} & B_{22} & B_{26} & D_{12} & D_{22} & D_{26} \\ B_{16} & B_{26} & B_{66} & D_{16} & D_{26} & D_{66} \end{bmatrix} \begin{bmatrix} \varepsilon_x \\ \varepsilon_y \\ \varepsilon_{xy} \\ \kappa_x \\ \kappa_y \\ \kappa_{xy} \end{bmatrix} \tag{10}$$

Assuming the lamellae are cross-sectionally symmetric, B_{ij}, A_{16}, and A_{26} can be set to 0. This assumption decouples rotation and extension matrices, simplifying the relations and enabling the computation of the effective elastic constants of the laminate, as shown in Eqns. (11)–(16).

$$\begin{bmatrix} \varepsilon_x \\ \varepsilon_y \\ \varepsilon_{xy} \end{bmatrix} = \begin{bmatrix} a_{11} & a_{12} & 0 \\ a_{12} & a_{22} & 0 \\ 0 & 0 & a_{66} \end{bmatrix} \begin{bmatrix} N_x \\ N_y \\ N_{xy} \end{bmatrix} \tag{11}$$

$$E_L = E_x = \frac{A_{11}A_{22}-A_{12}^2}{hA_{22}} \tag{12}$$

$$E_T = E_y = \frac{A_{11}A_{22}-A_{12}^2}{hA_{11}} \tag{13}$$

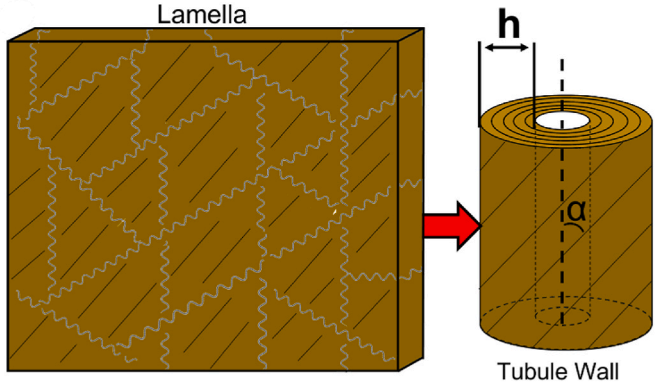

Fig. 5. Lamella within tubule wall laminate.

$$G_L = G_{xy} = \frac{A_{66}}{h} \tag{14}$$

$$\nu_L = \nu_{xy} = \frac{A_{12}}{A_{22}} \tag{15}$$

$$\nu_T = \nu_{yx} = \frac{A_{12}}{A_{11}} \tag{16}$$

where h stands for the total thickness of the laminate, and $[a]$ is the inverse of $[A]$ shown above.

3.4. Mesoscale

Fig. 6 illustrates the arrangement of tubules at the mesoscale. The hoof wall resembles a fiber-reinforced composite with the tubules as fibers and the intertubular material as the matrix. First, the effective longitudinal elastic modulus of a tubule is determined using the composite cylinders model to account for the empty space of the medullary cavity and the curvature of the tubule wall (Christensen, 2012).

$$E_c = f_1E_1 + (1-f_1)E_0 + \frac{4f_1(1-f_1)(\nu_1-\nu_0)^2G_0}{\frac{(1-f_1)G_0}{k_1+G_1/3}+\frac{f_1G_0}{k_0+G_0/3}+1} \tag{17}$$

The fiber, in this case, is a void with all elastic properties set to zero and the matrix is the tubule wall with the elastic properties of the laminate from the previous scale assuming isotropy. G and k represent the shear modulus and plane strain bulk modulus. With the properties of the fiber equal to zero, Eqn. (17) simplifies to the rule of mixtures. The Halpin-Tsai model is then used to calculate the effective properties of the hoof wall on the macroscale from the properties of the tubules and intertubular material.

4. Experimental inputs and assumptions

The models presented in Section 3 require inputs for the geometry and material properties of the components of the equine hoof wall. These inputs come from published experimental data. Some inputs are taken from experiments on other naturally occurring keratinous materials like wool and hagfish slime. This section discusses the assumptions made for the models and the inputs used.

The mechanical properties of keratin show a strong dependence on hydration level. Hydrated keratins exhibit lower stiffness and strength than dry keratins (Fraser and MacRae, 1983; Lazarus et al., 2021; Bertram and Gosline, 1987; Chapman, 1969; Feughelman, 1959). Experimentalists have accounted for this behavior by recording either the ambient relative humidity (RH) of the surroundings or the water content by weight (WC) of samples before conducting tests. WC is determined by comparing the weight of samples during a test to their dehydrated weight after oven drying. When the RH is used as a metric of the hydration level, it is assumed that the material has equilibrated with the surrounding humidity, and the hydration does not vary with time. The relationship between WC and RH for the hoof wall is shown in Fig. 7 (Bertram and Gosline, 1987). Experiments using different methods of controlling hydration can be directly compared using this data.

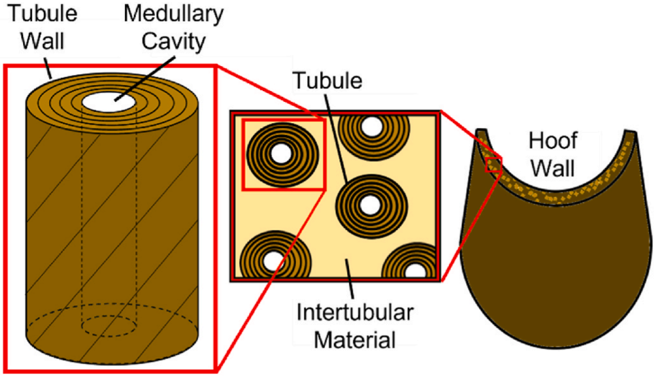

Fig. 6. Tubules within the hoof wall.

This paper considers two hydration levels based on the availability of experimental data. The first level is “dry,” which corresponds to a RH of 40% or 6–10% water by weight. The second level is “fully hydrated,” which corresponds to a RH of 100% or 35–45% water by weight. Each hydration level is a separate analysis with different experimental inputs that account for the softening of keratins in a hydrated state.

In addition to hydration effects, the properties of the hoof wall are sensitive to several other factors. Like other biological materials, keratin exhibits viscoelastic behavior. Therefore, measurements of the elastic properties of the hoof wall depend on the applied strain rate (Lazarus et al., 2021; Johnson et al., 2017; Kasapi and Gosline, 1996). Moreover, the properties and morphology of the equine hoof wall are anisotropic and not constant throughout the entire structure. The elastic modulus of the hoof wall differs in circumferential and radial directions (Lancaster et al., 2013) and the tubules at the inner wall are larger and less densely populated than those at the outer wall (Kasapi and Gosline, 1997; Leach, 1980; Bertram and Gosline, 1987; Lancaster et al., 2013; Douglas et al., 1996). For these reasons, the inputs used for the analysis must come from comparable experiments. Therefore, only experimental values from the toe region, midway between the outer and inner wall of the stratum medium, are used (Fig. 1). All experimentally obtained elastic properties come from quasi-static tension tests in the longitudinal direction except for the properties of the intertubular material which came from nanoindentation experiments.

4.1. Nanoscale

In most keratinous materials, it is difficult to evaluate the properties of the IFs and matrix phases separately. Luckily, a deep-sea dwelling animal called the hagfish excretes mucus as a defense mechanism that contains isolated strands of IF with no surrounding matrix material. The IF strands were mechanically tested underwater and in the air with an ambient RH of 40%. The initial tensile elastic modulus of the hagfish threads was 7.7 ± 0.5 GPa when dry (Fudge and Gosline, 2004) but only 6.4 ± 0.9 MPa (Fudge et al., 2003) when fully hydrated. However, these values do not fully capture the behavior of IF fibers in hard keratins such as wool, hair, or the equine hoof which do not show such significant change in mechanical properties in the presence of hydration. By comparing the swelling observed in fully hydrated hard keratins to the swelling of the fully hydrated hagfish threads, it is clear that when surrounded by the matrix material, the fibers do not absorb the same amount of water as they do in their exposed form as hagfish threads (Fudge et al., 2003). The hydration resistance of hard α-keratin IF fibers is hypothesized to result from the matrix restricting swelling of the

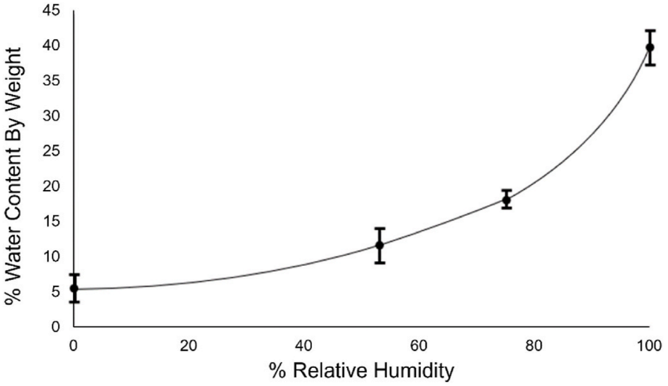

Fig. 7. Water absorption in the equine hoof wall.

fibers, keeping them relatively dry regardless of the hydration level (Wang et al., 2016a; Fudge et al., 2003). Therefore, the elastic modulus of the dry hagfish threads is used for the properties of the IFs in both the fully hydrated and dry analyses.

We are not aware of direct experiments measuring the properties of the matrix material in keratins. However, tests on wool in dry and hydrated states provide some insight into the properties of the matrix relative to the IF fibers. Wool strands tested in tension decrease in stiffness by less than a factor of 2 when fully hydrated, but when tested in torsion, the rigidity decreases by a factor of about 15 when fully hydrated (Feughelman, 1959). Based on these experiments, researchers have estimated that the matrix is about 13 times more compliant than the IF fibers in the fully hydrated condition. The matrix has approximately the same elastic modulus as the IF fibers in the dry condition (Feughelman, 1959). From these estimates, the elastic modulus of the matrix is assumed to be 7.7 GPa when dry and 585 MPa when fully hydrated. The sensitivity of the matrix's mechanical properties to hydration has been attributed to water forming plasticizing molecules or replacing hydrogen bonds in the proteins of the matrix (Wang et al., 2016a). The swelling of hydrated keratins can also affect their mechanical properties. However, according to measurements of the diametric swelling of keratins with different fractions of the matrix material, keratins with similar volume fractions to the equine hoof increase in volume up to 17% when fully hydrated (Greenberg and Fudge, 2013). The effect of swelling on the elastic modulus is then an order of magnitude smaller than effects due to molecular changes. Therefore, swelling of the material in the hydrated condition was not considered in this analysis. The same matrix material that fills the spaces between IFs is assumed to be present at several structural scales. So, the same elastic modulus and Poisson's ratio describe the matrix at the nano, sub-micro, and microscales.

Finally, the IFs are about 7 nm in diameter with 10 nm spacing between them (McKittrick et al., 2012; Huang et al., 2019), corresponding to a volume fraction of 44% within the macrofibrils. The Poisson's ratio for the fibers and matrix is assumed to be between 0.35 and 0.5 based on published estimates (Feughelman, 1959).

4.2. *Sub-microscale*

The diameter of macrofibrils in the equine hoof wall was measured using scanning electron microscopy (SEM) as 710 ± 130 nm (Huang et al., 2019). However, the volume fraction and length of these fibers are still unknown. The diameter of the cells (~20 μm) acts as a useful upper bound for the length of the macrofibrils, allowing them to be modeled as short fibers based on their maximum possible aspect ratio. The volume fraction of macrofibrils within the cells is also unknown. Still, birefringence measurements and SEM images of the hoof wall suggest that the total volume fraction of IF fibers in the tubular regions is about 22% (Kasapi and Gosline, 1999; Huang et al., 2019). Since the macrofibrils consist of 30% IF fibers by volume, the volume fraction of macrofibrils must be ~50%.

4.3. *Microscale*

The analytical model of suture interfaces used in this study assumes the cell's serrations have a regular trapezoidal shape. There is little data on the geometry of the cell interfaces. However, the total interface is approximately 750 nm wide with the cell boundary and intercellular space measuring about 15 nm and 30 nm across (Kasapi and Gosline, 1999). These values give an estimate of the sutures' amplitude and interface thickness, which are used to calculate the volume fraction of the serrations (90–93%) and interface material (7–10%). Values for the serration angle (37°–65°) and shape factor (10°–48°) were estimated from SEM images of the hoof cells by Huang et al. (2019). Finally, the model requires the interface material, which has not been characterized. Thus, the intercellular material is assumed to have identical elastic properties to the matrix phase in this analysis.

4.4. *Sub-mesoscale*

The lamellae in the tubule walls have varying fiber orientations determined by optical microscopy. The lamellae near the inner and outer sections of the tubule wall have higher winding angles (40°–60°) than the innermost lamellae (0°–20°) (Kasapi and Gosline, 1997). Using circularly polarized light micrographs and SEM images, the average thickness of the lamellae is measured as ~5–15 μm (Kasapi and Gosline, 1997; Huang et al., 2019).

4.5. *Mesoscale*

The mesoscale tubular structure of the hoof wall has been of interest to researchers for several decades, so the geometry and volume fraction of the tubules are well documented in the literature. Tubules from the middle section of the hoof typically have elliptical cross-sections with a major axis of 172–214 μm and a minor axis of 116–130 μm, with medullary cavities ranging from 32 to 50 μm in diameter (Kasapi and Gosline, 1997; Huang et al., 2019).

The final model also requires inputs for the elastic properties of the intertubular region. This material was isolated from the tubules and tested in tension underwater using a custom micro tension setup and was tested by nanoindentation under several hydration conditions. The reduced modulus of the intertubular region from nanoindentation tests was 7.0 ± 0.3 GPa for the dry condition, and 190 ± 20 MPa for the fully hydrated condition (Huang et al., 2019). In micro tension tests, the modulus of the fully hydrated intertubular material was 140 ± 50 MPa (Kasapi and Gosline, 1999). The Poisson's ratio has not been measured experimentally, so a range of 0.35–0.5 is used in the analysis. The volume fraction of the tubules relative to the intertubular region is 30% (Huang et al., 2019).

5. Validation

Measurements of the elastic properties of the equine hoof wall are available for the macroscale and mesoscale. These experimental values are used to validate the results of modeling.

Numerous studies have measured the tensile response of the hoof at the macroscale. The tensile elastic modulus in the toe region of the hoof wall at 100% RH ranges from 210 MPa to 490 MPa (Kasapi and Gosline, 1996, 1997; Bertram, 1984). There is no data for the elastic modulus of the hoof in tension at 40% RH; however, tensile tests at 53% RH give an elastic modulus of 3.36 ± 0.63 GPa (Bertram, 1984).

6. Results

The values presented in Table 2 are the complete set of parameters needed for modeling the hoof wall. The tensile modulus of hagfish threads served as the starting point for modeling the IFs at the nanoscale. Properties of the matrix were then derived from estimates of the ratio between the IF and matrix moduli. The necessary geometric parameters were taken from experimental characterizations of each structure or derived from assumptions and experimental data. Nanoindentation and micro tension tests on the intertubular material provide the matrix properties for the mesoscale Halpin-Tsai model.

Using these input parameters, the models discussed in Section 3 give predictions for the effective longitudinal moduli of the hoof wall's substructures. Each input value not derived from an assumption has some experimental uncertainty. The parameters in Table 2 with a plus-minus sign indicate the values that came from experiments that reported the standard deviation. The rest are reported in the literature as a range of measurements. The upper and lower bounds of elastic modulus were calculated for each scale from the uncertainties of experimental values and the output of the previous scale model. Fig. 8 compares

Table 2
Summary of experimental inputs for modeling.

Modeling Scale	Geometric Parameters		Material Properties		
			Property	40% RH	100% RH
Nano	IF volume fraction	44%[a], (McKittrick et al., 2012; Huang et al., 2019)	Fiber elastic modulus	7.7 ± 0.5 GPa (Fudge and Gosline, 2004)	7.7 ± 0.5 GPa (Fudge and Gosline, 2004)
			Fiber Poisson's ratio	0.35–0.5[a], (Feughelman, 1959)	0.35–0.5[a], (Feughelman, 1959)
			Matrix elastic modulus	7.7 GPa[a], (Feughelman, 1959; Fudge and Gosline, 2004)	585 MPa[a], (Feughelman, 1959; Fudge and Gosline, 2004)
			Matrix Poisson's ratio	0.4[a]	0.4[a]
Sub-micro	Macrofibril volume fraction	50%[a], (Kasapi and Gosline, 1999; Huang et al., 2019)	Matrix elastic modulus	[b]	[b]
	Macrofibril diameter	710 ± 130 nm[a], (Huang et al., 2019)	Matrix Poisson's ratio		
	Macrofibril length	1–20 μm[a], (Huang et al., 2019)		[b]	[b]
Micro	Serration volume fraction	90–93%[a], (Kasapi and Gosline, 1999)	Interface elastic modulus	[b]	[b]
	Serration angle				
	Shape factor	37°–65°[a], (Huang et al., 2019)	Interface Poisson's ratio		
		10°–48°[a], (Huang et al., 2019)		[b]	[b]
Sub-meso	Lamella thickness	5–15 μm (Kasapi and Gosline, 1997; Huang et al., 2019)			
Meso	Medullary cavity diameter	32–50 μm (Kasapi and Gosline, 1997; Huang et al., 2019)	Intertubular elastic modulus	5.9 ± 0.3 GPa (Huang et al., 2019)	160 ± 20 MPa (Huang et al., 2019)
	Tubule major diameter	172–214 μm (Kasapi and Gosline, 1997; Huang et al., 2019)	Intertubular Poisson's ratio		140 ± 50 MPa (Kasapi and Gosline, 1999)
	Tubule minor diameter	116–130 μm (Kasapi and Gosline, 1997; Huang et al., 2019)		0.35–0.5[a]	0.35–0.5[a]
	Tubule volume fraction	30% (Huang et al., 2019)			

[a] Value is not taken directly from the literature. One or more assumptions were used to determine value.
[b] Assumed to have properties equivalent to the matrix material present at the nanoscale.

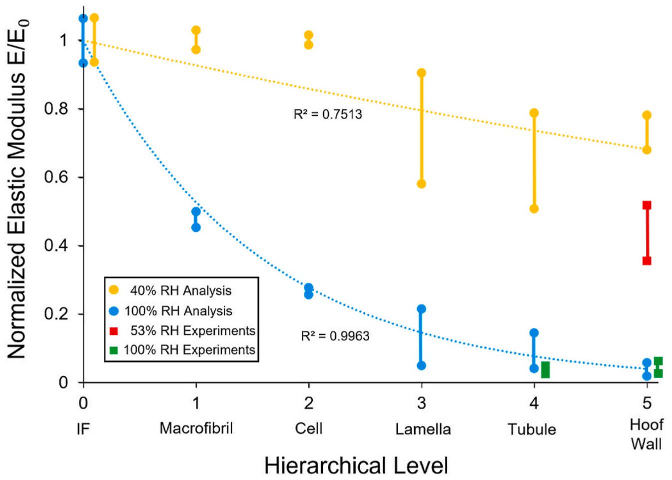

Fig. 8. Longitudinal elastic modulus of the hoof wall by structural scale, normalized by the elastic modulus of the 0th hierarchical level, the intermediate filament (IF).

experimental data with the results of modeling which were fit with exponential functions. The numerical values are listed in Table 3.

7. Discussion

The results of the analyses for the longitudinal elastic modulus of the hoof wall in tension match experiments well. Both the macroscale and mesoscale experimental values for the fully hydrated condition overlap with the range predicted by modeling. The results for the dry analysis show a higher predicted modulus than the available experimental data. However, there are no tension data for the hoof wall at 40% RH, so the macroscale results for the dry analysis are instead compared with the elastic modulus measured at 53% RH. Since the hoof softens with increasing hydration, the predicted values at 40% RH are expected to be higher than the experimental results at 53% RH.

Table 3
Longitudinal elastic modulus of hoof wall substructures in GPa.

	40% RH		100% RH	
Structure	Models	Experimental Validation Data	Models	Experimental Validation Data
IF	7.70 ± 0.50	–	7.70 ± 0.50	–
Macrofibril	7.70 ± 0.22	–	3.67 ± 0.18	–
Cell	7.70 ± 0.11	–	2.06 ± 0.08	–
Lamella	5.57 ± 1.37	–	1.00 ± 0.66	–
Tubule	4.85 ± 1.18	–	0.72 ± 0.41	0.29 ± 0.09 (Kasapi and Gosline, 1999)
Hoof Wall	5.59 ± 0.42	3.36 ± 0.629* (Bertram, 1984)	0.30 ± 0.15	0.410 ± 0.032 (Bertram, 1984) 0.28 ± 0.07 (Kasapi and Gosline, 1996) 0.43 ± 0.06 (Kasapi and Gosline, 1997)

*53% RH

The results given by the Halpin-Tsai model for the nano, sub-micro, and meso-scales fall between the bounds on the longitudinal elastic modulus of transversely isotropic composites obtained by Hill (Christensen, 2012; Hill, 1964):

$$\frac{f_1 f_2}{\frac{f_1}{K_2}+\frac{f_2}{K_1}+\frac{1}{\mu_1}} \leq \frac{E_c - f_1 E_1 - f_2 E_2}{4(\nu_1 - \nu_2)^2} \geq \frac{f_1 f_2}{\frac{f_1}{K_2}+\frac{f_2}{K_1}+\frac{1}{\mu_2}} \tag{18}$$

where E is longitudinal elastic modulus, K is plane strain bulk modulus, ν is Poisson's ratio, f is volume fraction, and the subscripts 1, 2, c indicate the two phases and the composite properties. When there is a small mismatch in elastic moduli between phases, the upper and lower bounds are very close and in the case of equal Poisson's ratios the bounds collapse to the rule of mixtures. Since the phases of keratin have similar elastic properties, the bounds follow the rule of mixtures within 5% even if a broader range of Poisson's ratios are considered. Therefore, uncertainty in the predictions for these scales is primarily due to the experimental inputs rather than the chosen model.

Both experimental and computed elastic moduli show a monotonic decrease with the spatial scale. This characteristic is not unique to hooves. A similar trend for elastic moduli was observed in an analysis of mineralized biological materials with structural hierarchy by Bechtle et al. (2010). Indeed, this decrease in moduli is connected to the increase in fracture toughness with the spatial scale, and is treated by the Yao-Gao theory of hierarchical levels (Yao and Gao, 2007), which concatenates the decrease in elastic modulus with the increase in fracture toughness. The latter is the result of interfaces between the different hierarchical levels, providing barriers to the propagation of cracks and introducing compliance. Thus, the decrease in the elastic modulus is inherently engineered into the hierarchical structures to provide enhanced toughness.

Despite using various composite material models at each level of hierarchy, a simple exponential decay of elastic modulus with increasing spatial scale fits the results well for both hydration conditions. This makes intuitive sense given the decrease in fiber volume fraction and additional compliance for each successive hierarchical level. The predictive power of the models can be improved by generalizing the exponential fit to other hydration levels. Assuming a linear change of the exponent with a change in relative humidity, one can write an expression for the longitudinal elastic modulus which depends on the hierarchical level (n) and percent ambient relative humidity (RH).

$$E_n = E_0 * \exp\left[(0.293 - 0.009RH)n\right] \tag{19}$$

The empirical exponential model, shown in Fig. 9, agrees reasonably well with experiments for 53% and 75% RH with 0 and 55 percent error, respectively. However, the model overpredicts the macroscale modulus at 0% RH and predicts an increase in elastic modulus with additional hierarchical levels at humidities lower than 40%, which is an unphysical result. This could be due to the assumption that the IF modulus, measured at 40% RH, remains constant for all hydration conditions. The IFs may exhibit higher moduli when there is almost no water present, which explains how the experimentally measured modulus of the hoof wall at 0% RH can be almost twice that obtained from dry hagfish threads. Still, the results of this analysis, validated at the macroscale and mesoscale for a hydrated hoof wall, support the notion that the matrix is primarily responsible for the variation in properties due to hydration effects.

This study has limitations due to the paucity of experimental measurements. Every model used in the analysis is valid for the elastic properties in tension. However, the properties obtained from nanoindentation are more representative of the local material behavior in compression. This could lead to errors in the macroscale predictions since results from nanoindentation were used as inputs for the properties of the intertubular material.

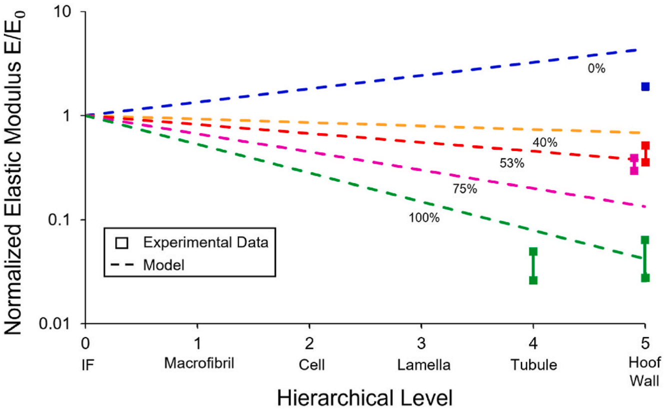

Fig. 9. Predicted elastic moduli by hierarchical level and ambient relative humidity.

More experimental data is needed to validate or improve the models used in this study for future work. The accuracy of the models at lower length scales will remain unknown without experimental data for the macrofibrils, cells, lamellae, and more complete data at all scales. Micromechanical modeling of these structures can also further validate the results and expand on them to include behavior beyond the linear elastic region. Finally, one of the main interests in studying the hoof wall is its impact resistance. The hierarchical structure of the hoof wall likely plays a role in the overall dynamic behavior. So, understanding the structure-property relations of the hoof wall at different scales under dynamic loading will be essential to efforts in hoof-inspired impact-resistant designs. Thus, dynamic testing and modeling are needed. Viscoelastic properties at the macroscale and mesoscale can be obtained through experiments such as dynamic mechanical analysis (DMA) and nano-DMA and used to understand the time-dependent response of the hoof's substructures in a top-down approach. The current study sets a framework for such extensions.

In summary, this paper utilized micromechanics tools developed for composite materials to compute the structure-property relations for the equine hoof wall. The novelty is in the proposed experimentally based hierarchical model of a hoof wall in which we use one or more models for each scale and test their validity by comparing them with experimental data. Secondly, this approach can serve as a framework for more realistic analytical or numerical hierarchical models of a hoof wall accounting for viscoelastic, viscoplastic, and nonlinear effects.

8. Conclusions

The hierarchical structure of a hoof wall contributes to its superior mechanical performance, such as high impact and fracture resistance. This paper addresses the structure-property relations for the equine hoof wall at different length scales. The length scales studied include the macroscale hoof wall, mesoscale tubules (0.1–0.5 mm), sub-mesoscale lamellae (10–50 μm), microscale cells (1–20 μm), sub-microscale macrofibrils (0.5–1 μm), and nanoscale IFs (1–10 nm). A series of experimentally based, analytical models, assuming linear elastic properties of phases, were employed to model the longitudinal elastic modulus at each structural scale of the horse hoof wall for two hydration conditions (40% RH and 100% RH) and the results were generalized to other hydration conditions.

The macroscale and mesoscale results have been validated with the existing experimental data. The results provide new insights into the elastic behavior of structures in the hoof wall, particularly at the lower scales that are challenging to test experimentally. The linear elastic formulations are a starting point for more advanced hierarchical models of an equine hoof wall accounting for nonlinear and time-dependent effects. This study also can serve as a framework for designing hoof-inspired materials and structures.

CRediT authorship contribution statement

Cheng-Shen (Andrew) Shiang: Writing – review & editing, Writing – original draft, Visualization, Validation, Methodology, Investigation, Formal analysis, Data curation, Conceptualization. **Christian Bonney:** Writing – review & editing, Visualization, Validation, Methodology, Investigation, Formal analysis, Data curation. **Benjamin Lazarus:** Writing – review & editing, Methodology, Investigation, Formal analysis. **Marc Meyers:** Writing – review & editing, Supervision, Project administration, Methodology, Investigation. **Iwona Jasiuk:** Writing – review & editing, Supervision, Resources, Project administration, Methodology, Investigation, Funding acquisition, Formal analysis, Conceptualization.

Declaration of competing interest

The authors declare that they have no known competing financial interests or personal relationships that could have appeared to influence the work reported in this paper.

Data availability

Data will be made available on request.

Acknowledgments

This research has been supported by funding from the National Science Foundation Mechanics of Materials and Structures program (Grant numbers 1926353 and 1926361). We dedicate this paper to Prof. Joanna McKittrick's memory.

References

Achrai, B., Wagner, H.D., 2013. Micro-structure and mechanical properties of the turtle carapace as a biological composite shield. Acta Biomater. 9 (4), 5890–5902. https://doi.org/10.1016/j.actbio.2012.12.023.

Ampaw, E., Owoseni, T.A., Du, F., Pinilla, N., Obayemi, J., Hu, J., Nigay, P.-M., Nzihou, A., Uzonwanne, V., Zebaze-Kana, M.G., 2019. Compressive deformation and failure of trabecular structures in a turtle shell. Acta Biomater. 97, 535–543. https://doi.org/10.1016/j.actbio.2019.07.023.

Azzi, V.D., Tsai, S., 1965. Elastic moduli of laminated anisotropic composites. Exp. Mech. 5 (6), 177–185. https://doi.org/10.1007/BF02328424.

Bechtle, S., Ang, S.F., Schneider, G.A., 2010. On the mechanical properties of hierarchically structured biological materials. Biomaterials 31 (25), 6378–6385. https://doi.org/10.1016/j.biomaterials.2010.05.044.

Bertram, J.E., 1984. Fracture Toughness Design in Equine Hoof Wall. University of British Columbia.

Bertram, J.E., Gosline, J.M., 1986. Fracture toughness design in horse hoof keratin. J. Exp. Biol. 125 (1), 29–47. https://doi.org/10.1242/jeb.125.1.29.

Bertram, J., Gosline, J., 1987. Functional design of horse hoof keratin: the modulation of mechanical properties through hydration effects. J. Exp. Biol. 130 (1), 121–136. https://doi.org/10.1242/jeb.130.1.121.

Brown, A.D., Rafaels, K.A., Weerasooriya, T., 2020. Microstructural and Rate-dependent Shear Response of Human Skull Bones. CCDC Army Research Laboratory Aberdeen Proving Ground United States.

Chapman, B., 1969. 15—a review of the mechanical properties of keratin fibres. J. Textil. Inst. 60 (5), 181–207. https://doi.org/10.1080/00405006908629920.

Chen, I.H., Yang, W., Meyers, M.A., 2015. Leatherback sea turtle shell: a tough and flexible biological design. Acta Biomater. 28, 2–12. https://doi.org/10.1016/j.actbio.2015.09.023.

Chen, B., Zou, M., Liu, G., Song, J., Wang, H., 2018. Experimental study on energy absorption of bionic tubes inspired by bamboo structures under axial crushing. Int. J. Impact Eng. 115, 48–57. https://doi.org/10.1016/j.ijimpeng.2018.01.005.

Christensen, R.M., 2012. Mechanics of Composite Materials. Courier Corporation.

Cordisco, F.A., Zavattieri, P.D., Hector Jr., L.G., Bower, A.F., 2012. Toughness of a patterned interface between two elastically dissimilar solids. Eng. Fract. Mech. 96, 192–208. https://doi.org/10.1016/j.engfracmech.2012.07.018.

Cordisco, F., Zavattieri, P.D., Hector Jr., L.G., Bower, A.F., 2014. On the mechanics of sinusoidal interfaces between dissimilar elastic–plastic solids subject to dominant mode I. Eng. Fract. Mech. 131, 38–57. https://doi.org/10.1016/j.engfracmech.2014.06.004.

Crick, F.H., 1952. Is α-keratin a coiled coil? Nature 170 (4334), 882–883. https://doi.org/10.1038/170882b0.

Cui, Y., Gong, H., Wang, Y., Li, D., Bai, H., 2018. A thermally insulating textile inspired by polar bear hair. Adv. Mater. 30 (14), 1706807 https://doi.org/10.1002/adma.201706807.

Dimitrienko, Y.I., Dimitrienko, I., Sborschikov, S., 2015. Multiscale hierarchical modeling of fiber reinforced composites by asymptotic homogenization method. Appl. Math. Sci. 9 (145), 7211–7220. https://doi.org/10.12988/ams.2015.510641.

Douglas, J., Mittal, C., Thomason, J., Jofriet, J., 1996. The modulus of elasticity of equine hoof wall: implications for the mechanical function of the hoof. J. Exp. Biol. 199 (8), 1829–1836. https://doi.org/10.1242/jeb.199.8.1829.

Dunlop, J.W., Weinkamer, R., Fratzl, P., 2011. Artful interfaces within biological materials. Mater. Today 14 (3), 70–78. https://doi.org/10.1016/S1369-7021(11)70056-6.

Feughelman, M., 1959. A two-phase structure for keratin fibers. Textil. Res. J. 29 (3), 223–228 https://doi.org/10.1177%2F004051755902900305.

Fraser, R., MacRae, T., 1983. The structure of the α-keratin microfibril. Biosci. Rep. 3 (6), 517–525. https://doi.org/10.1007/BF01120695.

Fudge, D.S., Gosline, J.M., 2004. Molecular design of the α–keratin composite: insights from a matrix–free model, hagfish slime threads. Proc. R. Soc. Lond. Ser. B Biol. Sci. 271 (1536), 291–299. https://doi.org/10.1098/rspb.2003.2591.

Fudge, D.S., Gardner, K.H., Forsyth, V.T., Riekel, C., Gosline, J.M., 2003. The mechanical properties of hydrated intermediate filaments: insights from hagfish slime threads. Biophys. J. 85 (3), 2015–2027. https://doi.org/10.1016/S0006-3495(03)74629-3.

Ghazlan, A., Ngo, T.D., Tran, P., 2016. Three-dimensional Voronoi model of a nacre-mimetic composite structure under impulsive loading. Compos. Struct. 153, 278–296. https://doi.org/10.1016/j.compstruct.2016.06.020.

Greenberg, D.A., Fudge, D.S., 2013. Regulation of hard α-keratin mechanics via control of intermediate filament hydration: matrix squeeze revisited. Proc. Biol. Sci. 280 (1750), 20122158 https://doi.org/10.1098/rspb.2012.2158.

Grunenfelder, L., Suksangpanya, N., Salinas, C., Milliron, G., Yaraghi, N., Herrera, S., Evans-Lutterodt, K., Nutt, S., Zavattieri, P., Kisailus, D., 2014. Bio-inspired impact-resistant composites. Acta Biomater. 10 (9), 3997–4008. https://doi.org/10.1016/j.actbio.2014.03.022.

Gu, G.X., Takaffoli, M., Buehler, M.J., 2017. Hierarchically enhanced impact resistance of bioinspired composites. Adv. Mater. 29 (28), 1700060 https://doi.org/10.1002/adma.201700060.

Halpin, J., 1969. Stiffness and expansion estimates for oriented short fiber composites. J. Compos. Mater. 3 (4), 732–734. https://doi.org/10.1177/002199836900300419.

Halpin, J.C., Kardos, J.L., 1976. The Halpin-Tsai equations: a review. Polym. Eng. Sci. 16 (5), 344–352. https://doi.org/10.1002/pen.760160512.

Hamed, E., Lee, Y., Jasiuk, I., 2010. Multiscale modeling of elastic properties of cortical bone. Acta Mech. 213 (1), 131–154. https://doi.org/10.1007/s00707-010-0326-5.

Hao, P., Du, J., 2018. Mechanical properties of bio-mimetic energy-absorbing materials under impact loading. J. Mater. Sci. 53 (5), 3189–3197. https://doi.org/10.1007/s10853-017-1798-7.

Hill, R., 1964. Theory of mechanical properties of fibre-strengthened materials: I. Elastic behaviour. J. Mech. Phys. Solid. 12 (4), 199–212.

Huang, W., 2018. Impact Resistant and Energy Absorbent Natural Keratin Materials: Horns and Hooves. University of California, San Diego.

Huang, W., Yaraghi, N.A., Yang, W., Velazquez-Olivera, A., Li, Z., Ritchie, R.O., Kisailus, D., Stover, S.M., McKittrick, J., 2019. A natural energy absorbent polymer composite: the equine hoof wall. Acta Biomater. 90, 267–277. https://doi.org/10.1016/j.actbio.2019.04.003.

Hyer, M.W., White, S.R., 2009. Stress Analysis of Fiber-Reinforced Composite Materials. DEStech Publications, Inc.

Islam, M.K., Wang, H., Hazell, P.J., Kader, M.A., Escobedo, J.P., 2022. Quasi-static response of horse hoof inspired biomimetic structures, Materials Today. Proceedings. https://doi.org/10.1016/j.matpr.2022.03.185.

Jia, Z., Yu, Y., Hou, S., Wang, L., 2019. Biomimetic architected materials with improved dynamic performance. J. Mech. Phys. Solid. 125, 178–197. https://doi.org/10.1016/j.jmps.2018.12.015.

Jiang, H., Ghods, S., Ma, Y., Dai, X., Yang, F., He, X., 2020. Designed for the enhancement of structure mechanostability and strength: suture-serrate margins of bivalve shells. J. Mech. Behav. Biomed. Mater. 103, 103586 https://doi.org/10.1016/j.jmbbm.2019.103586.

Johnson, K., Trim, M., Francis, D., Whittington, W., Miller, J., Bennett, C., Horstemeyer, M., 2017. Moisture, anisotropy, stress state, and strain rate effects on bighorn sheep horn keratin mechanical properties. Acta Biomater. 48, 300–308. https://doi.org/10.1016/j.actbio.2016.10.033.

Kasapi, M.A., Gosline, J.M., 1996. Strain-rate-dependent mechanical properties of the equine hoof wall. J. Exp. Biol. 199 (5), 1133–1146. https://doi.org/10.1242/jeb.199.5.1133.

Kasapi, M.A., Gosline, J.M., 1997. Design complexity and fracture control in the equine hoof wall. J. Exp. Biol. 200 (11), 1639–1659. https://doi.org/10.1242/jeb.200.11.1639.

Kasapi, M.A., Gosline, J.M., 1999. Micromechanics of the equine hoof wall: optimizing crack control and material stiffness through modulation of the properties of keratin. J. Exp. Biol. 202 (4), 377–391. https://doi.org/10.1242/jeb.202.4.377.

Kwon, Y., Clumpner, B., 2018. Multiscale modeling of human bone. Multiscale and Multidisciplinary Modeling, Experiments and Design 1 (2), 133–143. https://doi.org/10.1007/s41939-018-0013-0.

Lancaster, L.S., Bowker, R.M., Mauer, W.A., 2013. Equine hoof wall tubule density and morphology. J. Vet. Med. Sci. 12. https://doi.org/10.1292/jvms.12-0399, 0399.

Lanovaz, J., Clayton, H., Watson, L., 1998. In vitro attenuation of impact shock in equine digits. Equine Vet. J. 30 (S26), 96–102. https://doi.org/10.1111/j.2042-3306.1998.tb05127.x.

Launey, M.E., Chen, P.-Y., McKittrick, J., Ritchie, R., 2010. Mechanistic aspects of the fracture toughness of elk antler bone. Acta Biomater. 6 (4), 1505–1514. https://doi.org/10.1016/j.actbio.2009.11.026.

Lazarus, B.S., Velasco-Hogan, A., Gómez-del Río, T., Meyers, M.A., Jasiuk, I., 2020. A review of impact resistant biological and bioinspired materials and structures. J. Mater. Res. Technol. 9 (6), 15705–15738. https://doi.org/10.1016/j.jmrt.2020.10.062.

Lazarus, B.S., Chadha, C., Velasco-Hogan, A., Barbosa, J.D., Jasiuk, I., Meyers, M.A., 2021. Engineering with keratin: a functional material and a source of bioinspiration. iScience 24 (8), 102798. https://doi.org/10.1016/j.isci.2021.102798.

Leach, D., 1980. The Structure and Function of the Equine Hoof Wall.

Lee, S., Novitskaya, E.E., Reynante, B., Vasquez, J., Urbaniak, R., Takahashi, T., Woolley, E., Tombolato, L., Chen, P.-Y., McKittrick, J., 2011. Impact testing of structural biological materials. Mater. Sci. Eng. C 31 (4), 730–739. https://doi.org/10.1016/j.msec.2010.10.017.

Li, Y., Ortiz, C., Boyce, M.C., 2011. Stiffness and strength of suture joints in nature. Phys. Rev. 84 (6), 062904 https://doi.org/10.1103/PhysRevE.84.062904.

Li, Y., Ortiz, C., Boyce, M.C., 2012. Bioinspired, mechanical, deterministic fractal model for hierarchical suture joints. Phys. Rev. 85 (3), 031901 https://doi.org/10.1103/PhysRevE.85.031901.

Li, Y., Ortiz, C., Boyce, M.C., 2013. A generalized mechanical model for suture interfaces of arbitrary geometry. J. Mech. Phys. Solid. 61 (4), 1144–1167. https://doi.org/10.1016/j.jmps.2012.10.004.

Lin, A., Meyers, M.A., 2005. Growth and structure in abalone shell. Mater. Sci. Eng., A 390 (1–2), 27–41. https://doi.org/10.1016/j.msea.2004.06.072.

Lin, E., Li, Y., Ortiz, C., Boyce, M.C., 2014a. 3D printed, bio-inspired prototypes and analytical models for structured suture interfaces with geometrically-tuned deformation and failure behavior. J. Mech. Phys. Solid. 73, 166–182. https://doi.org/10.1016/j.jmps.2014.08.011.

Lin, E., Li, Y., Weaver, J.C., Ortiz, C., Boyce, M.C., 2014b. Tunability and enhancement of mechanical behavior with additively manufactured bio-inspired hierarchical suture interfaces. J. Mater. Res. 29 (17), 1867–1875. https://doi.org/10.1557/jmr.2014.175.

Liu, L., Jiang, Y., Boyce, M., Ortiz, C., Baur, J., Song, J., Li, Y., 2017. The effects of morphological irregularity on the mechanical behavior of interdigitated biological sutures under tension. J. Biomech. 58, 71–78. https://doi.org/10.1016/j.jbiomech.2017.04.017.

Liu, Z., Zhang, Z., Ritchie, R.O., 2020. Interfacial toughening effect of suture structures. Acta Biomater. 102, 75–82. https://doi.org/10.1016/j.actbio.2019.11.034.

Ma, W., Xie, S., Li, Z., Feng, Z., Jing, K., 2021. Crushing behaviors of horse-hoof-wall inspired corrugated tubes under multiple loading conditions. Mech. Adv. Mater. Struct. 1–25. https://doi.org/10.1080/15376494.2021.1892245.

Marshall, R.C., Orwin, D.F., Gillespie, J., 1991. Structure and biochemistry of mammalian hard keratin. Electron. Microsc. Rev. 4 (1), 47–83. https://doi.org/10.1016/0892-0354(91)90016-6.

Matsushita, A., Gonzalez, D., Wang, M., Doan, J., Qiao, Y., McKittrick, J., 2020. Beyond density: mesostructural features of impact resistant wood. Mater. Today Commun. 22, 100697 https://doi.org/10.1016/j.mtcomm.2019.100697.

McKittrick, J., Chen, P.-Y., Bodde, S., Yang, W., Novitskaya, E., Meyers, M., 2012. The structure, functions, and mechanical properties of keratin. JOM 64 (4), 449–468. https://doi.org/10.1007/s11837-012-0302-8.

Meyers, M.A., Chen, P.-Y., Lin, A.Y.-M., Seki, Y., 2008. Biological materials: structure and mechanical properties. Prog. Mater. Sci. 53 (1), 1–206. https://doi.org/10.1016/j.pmatsci.2007.05.002.

Miranda, P., Pajares, A., Meyers, M.A., 2019. Bioinspired composite segmented armour: numerical simulations. J. Mater. Res. Technol. 8 (1), 1274–1287. https://doi.org/10.1016/j.jmrt.2018.09.007.

Osoka, E., Onukwuli, O., 2018. A modified Halpin-Tsai model for estimating the modulus of natural fiber reinforced composites. International Journal of Engineering Science Invent 7 (5), 63–70.

Piat, R., Schnack, E., 2003. Hierarchical material modeling of carbon/carbon composites. Carbon 41 (11), 2121–2129. https://doi.org/10.1016/S0008-6223(03)00240-9.

Ramírez-Torres, A., Penta, R., Rodríguez-Ramos, R., Merodio, J., Sabina, F.J., Bravo-Castillero, J., Guinovart-Díaz, R., Preziosi, L., Grillo, A., 2018. Three scales asymptotic homogenization and its application to layered hierarchical hard tissues. Int. J. Solid Struct. 130, 190–198. https://doi.org/10.1016/j.ijsolstr.2017.09.035.

Ramírez-Torres, A., Penta, R., Rodríguez-Ramos, R., Grillo, A., 2019. Effective properties of hierarchical fiber-reinforced composites via a three-scale asymptotic homogenization approach. Math. Mech. Solid 24 (11), 3554–3574. https://doi.org/10.1177/1081286519847687.

Rice, C., Tan, K., 2019. Horse hoof inspired biomimetic structure for improved damage tolerance and crack diversion. Compos. Struct. 220, 362–370. https://doi.org/10.1016/j.compstruct.2019.04.009.

Rivera, J., Hosseini, M.S., Restrepo, D., Murata, S., Vasile, D., Parkinson, D.Y., Barnard, H.S., Arakaki, A., Zavattieri, P., Kisailus, D., 2020. Toughening mechanisms of the elytra of the diabolical ironclad beetle. Nature 586 (7830), 543–548. https://doi.org/10.1038/s41586-020-2813-8.

Setterbo, J.J., Garcia, T.C., Campbell, I.P., Reese, J.L., Morgan, J.M., Kim, S.Y., Hubbard, M., Stover, S.M., 2009. Hoof accelerations and ground reaction forces of Thoroughbred racehorses measured on dirt, synthetic, and turf track surfaces. Am. J. Vet. Res. 70 (10), 1220–1229. https://doi.org/10.2460/ajvr.70.10.1220.

Shahkhosravi, N.A., Gohari, S., Komeili, A., Burvill, C., Davies, H., 2021. Linear elastic and hyperelastic studies of equine hoof mechanical response at different hydration levels. J. Mech. Behav. Biomed. Mater. 121, 104622 https://doi.org/10.1016/j.jmbbm.2021.104622.

Toni, M., Dalla Valle, L., Alibardi, L., 2007. Hard (beta-) keratins in the epidermis of reptiles: composition, sequence, and molecular organization. J. Proteome Res. 6 (9), 3377–3392. https://doi.org/10.1021/pr0702619.

Tsang, H., Raza, S., 2018. Impact energy absorption of bio-inspired tubular sections with structural hierarchy. Compos. Struct. 195, 199–210. https://doi.org/10.1016/j.compstruct.2018.04.057.

Wang, B., Yang, W., McKittrick, J., Meyers, M.A., 2016a. Keratin: structure, mechanical properties, occurrence in biological organisms, and efforts at bioinspiration. Prog. Mater. Sci. 76, 229–318. https://doi.org/10.1016/j.pmatsci.2015.06.001.

Wang, B., Yang, W., Sherman, V.R., Meyers, M.A., 2016b. Pangolin armor: overlapping, structure, and mechanical properties of the keratinous scales. Acta Biomater. 41, 60–74. https://doi.org/10.1016/j.actbio.2016.05.028.

Wang, B., Sullivan, T.N., Pissarenko, A., Zaheri, A., Espinosa, H.D., Meyers, M.A., 2019. Lessons from the ocean: whale baleen fracture resistance. Adv. Mater. 31 (3), 1804574 https://doi.org/10.1002/adma.201804574.

Wang, B., Zhou, B., Zhang, X., 2020a. A high toughness and light weight armor structure bioinspired design based on a bovine hoof wall. Mater. Lett. 264, 127296 https://doi.org/10.1016/j.matlet.2020.127296.

Wang, B., Zhou, B., Zhang, X., Wang, B., 2020b. Microstructure and mechanical properties of an alpha keratin bovine hoof wall. J. Mech. Behav. Biomed. Mater. 104, 103689 https://doi.org/10.1016/j.jmbbm.2020.103689.

Wang, B., Huang, Y., Zhou, B., Li, W., Chen, H., 2021. Nanoindentation and hierarchy structure of the bovine hoof ll. Materials 14 (2), 289. https://doi.org/10.3390/ma14020289.

Yang, W., Naleway, S.E., Porter, M.M., Meyers, M.A., McKittrick, J., 2015. The armored carapace of the boxfish. Acta Biomater. 23, 1–10. https://doi.org/10.1016/j.actbio.2015.05.024.

Yao, H., Gao, H., 2007. Multi-scale cohesive laws in hierarchical materials. Int. J. Solid Struct. 44 (25–26), 8177–8193. https://doi.org/10.1016/j.ijsolstr.2007.06.007.

Yu, Y., Yang, W., Wang, B., Meyers, M.A., 2017. Structure and mechanical behavior of human hair. Mater. Sci. Eng. C 73, 152–163. https://doi.org/10.1016/j.msec.2016.12.008.

Zhang, L., Bai, Z., Bai, F., 2018. Crashworthiness design for bio-inspired multi-cell tubes with quadrilateral, hexagonal and octagonal sections. Thin-Walled Struct. 122, 42–51. https://doi.org/10.1016/j.tws.2017.10.010.